

# A pH-Responsive Yolk-Like Nanoplatfom for Tumor Targeted Dual-Mode Magnetic Resonance Imaging and Chemotherapy

Xiao Sun,<sup>†,‡,¶,||</sup> Ruohong Du,<sup>§,¶</sup> Li Zhang,<sup>∇,¶</sup> Guilong Zhang,<sup>†</sup> Xiaojia Zheng,<sup>○</sup> Junchao Qian,<sup>⊥</sup> Xiaohe Tian,<sup>#</sup> Jiewen Zhou,<sup>||</sup> Jiakai He,<sup>○</sup> Yuanyin Wang,<sup>○</sup> Yiqun Wu,<sup>||</sup> Kai Zhong,<sup>⊥</sup> Dongqing Cai,<sup>\*,†</sup> Duohong Zou,<sup>\*,||</sup> and Zhengyan Wu<sup>\*,†,¶</sup>

<sup>†</sup>Key Laboratory of Ion Beam Bioengineering, Hefei Institutes of Physical Science, Chinese Academy of Sciences, Hefei 230031, P.R. China

<sup>‡</sup>University of Chinese Academy of Sciences, Beijing 100049, P.R. China

<sup>§</sup>Department of Stomatology and <sup>∇</sup>Department of Urology, The First Affiliated Hospital of Anhui Medical University, Hefei 230022, P.R. China

<sup>○</sup>Dental Implant Center, Stomatologic Hospital and College, Key Laboratory of Oral Diseases Research of Anhui Province, Anhui Medical University, Hefei 230032, P.R. China

<sup>||</sup>Second Dental Clinic, School of Medicine, Shanghai Key Laboratory of Stomatology, Ninth People's Hospital Affiliated with Shanghai Jiao Tong University, Shanghai 200001, P.R. China

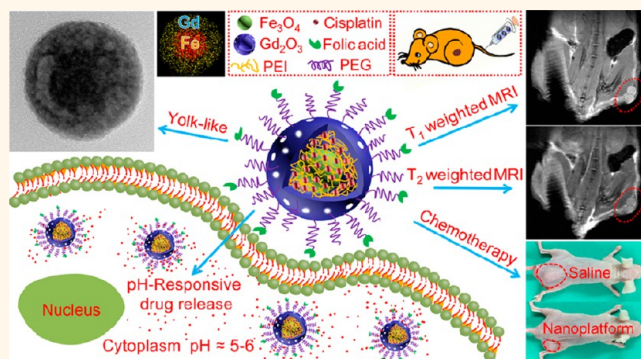
<sup>⊥</sup>High Magnetic Field Laboratory, Hefei Institutes of Physical Science, Chinese Academy of Sciences, Hefei 230031, P.R. China

<sup>#</sup>School of Life Sciences, Anhui University, Hefei 230601, P.R. China

## S Supporting Information

**ABSTRACT:** Incorporation of T<sub>1</sub> and T<sub>2</sub> contrast material in one nanosystem performing their respective MR contrast role and simultaneously serving as an efficient drug delivery system (DDS) has a significant potential application for clinical diagnosis and chemotherapy of cancer. However, inappropriate incorporation always encountered many issues, such as low contact area of T<sub>1</sub> contrast material with water-proton, inappropriate distance between T<sub>2</sub> contrast material and water molecule, and undesirable disturbance of T<sub>2</sub> contrast material for T<sub>1</sub> imaging. Those issues seriously limited the T<sub>1</sub> or T<sub>2</sub> contrast effect. In this work, we developed a yolk-like Fe<sub>3</sub>O<sub>4</sub>@Gd<sub>2</sub>O<sub>3</sub> nanoplatfom functionalized by polyethylene glycol and folic acid (FA), which could efficiently exert their tumor targeted T<sub>1</sub>-T<sub>2</sub> dual-mode MR imaging and drug delivery role. First, this nanoplatfom possessed a high longitudinal relaxation rate ( $r_1$ ) (7.91 mM<sup>-1</sup> s<sup>-1</sup>) and a stronger transverse relaxation rate ( $r_2$ ) (386.5 mM<sup>-1</sup> s<sup>-1</sup>) than that of original Fe<sub>3</sub>O<sub>4</sub> (268.1 mM<sup>-1</sup> s<sup>-1</sup>). Second, cisplatin could be efficiently loaded into this nanoplatfom (112 mg/g) and showed pH-responsive release behavior. Third, this nanoplatfom could be effectively internalized by HeLa cells with time and dosage dependence. Fourth, the FA receptor-mediated nanoplatfom displayed excellent T<sub>1</sub>-T<sub>2</sub> dual mode MR contrast enhancement and anticancer activity both *in vitro* and *in vivo*. Fifth, no apparent toxicity for vital organs was observed with systemic delivery of the nanoplatfom *in vivo*. Thus, this nanoplatfom could be a potential nanotheranostic for tumor targeted T<sub>1</sub>-T<sub>2</sub> dual-mode MR imaging and chemotherapy.

**KEYWORDS:** yolk-like Fe<sub>3</sub>O<sub>4</sub>@Gd<sub>2</sub>O<sub>3</sub>, targeted, dual-mode MR imaging, drug delivery system, cisplatin, pH responsive, cancer chemotherapy



Magnetic resonance imaging (MRI) is one of the most powerful diagnostic tools for detecting tumors due to its non-ionizing radiation, high spatial resolution, and non-limited penetration depth.<sup>1,2</sup> Approximately 50% of

Received: April 17, 2017

Accepted: June 30, 2017

Published: June 30, 2017

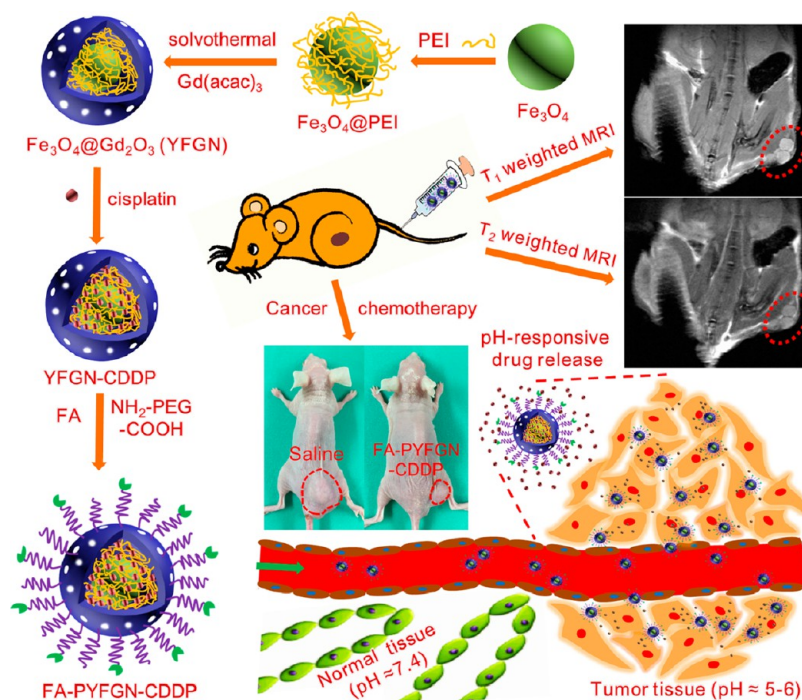


**Figure 1.** Schematic illustration of the fabrication process, systemic delivery of FA-PYFGN-CDDP *in vivo*, and corresponding diagnosis and therapy for tumor.

clinical MR examinations require use of contrast agent (CA) to enhance the quality of images.<sup>3,4</sup> CA can be divided into two types: Gd-based compound ( $T_1$  mode) and Fe-based magnetic nanoparticle ( $T_2$  mode). However, each type of CA contains inherent limitations (*i.e.*, short blood circulation time for  $T_1$  CA and magnetic susceptibility artifacts for  $T_2$  CA).<sup>5–8</sup>

Currently, MRI CA with dual functions ( $T_1$ – $T_2$  mode) have attracted considerable interests because it can combine advantages in both  $T_1$  and  $T_2$  CA.<sup>9–11</sup> To obtain dual mode CA, an effective way can be developed by combining Gd- and Fe-based compounds into one nanosystem.<sup>5,12</sup> As previously established, the contrast ability of  $T_1$  CA was related to the contact area between CA and water molecules,<sup>13,14</sup> and  $T_2$  CA was related to the distance between CA and water molecules.<sup>15,16</sup> Thus, (1) the higher contact area between  $T_1$  CA and water protons and (2) the closer distance between  $T_2$  CA and water molecules will facilitate better  $T_1$  and  $T_2$  imaging, respectively. It is worth noting that in the case of magnetic core directly contacting with  $T_1$  CA, the magnetic field generated by a magnetic core can perturb the relaxation process of the paramagnetic  $T_1$  CA, which can cause the decrease in  $T_1$  contrast ability.<sup>16–18</sup> Therefore, gadolinium ions need to be separated from the magnetic core to reduce this disturbance. So far, the format combining gadolinium-species and magnetic core into one nanosystem mainly included gadolinium-grafted,<sup>5,19,20</sup> coated, or doped  $Fe_3O_4$ ,<sup>6,7,12,21–23</sup> and gadolinium-grafted or coated  $Fe_3O_4@SiO_2$ ,<sup>8,16,17</sup> *etc.* However, these formulations encountered different problems (*i.e.*, low contact area of gadolinium with water-proton, inappropriate distance between  $Fe_3O_4$  and water molecule, or undesirable disturbance of  $Fe_3O_4$  for gadolinium), so that their  $T_1$  or  $T_2$  contrast effect was seriously limited and could not simultaneously exert their functions. To resolve these issues, we speculated that  $Fe_3O_4@Gd_2O_3$  nanoparticle with yolk-like structure might be beneficial to obtain excellent  $T_1$ – $T_2$  dual-mode MR imaging. The porous  $Gd_2O_3$  shell would have a high contact area with water protons,

which could facilitate effective  $T_1$  imaging. Meanwhile, water molecules could easily pass through the porous shell and approach the surface of  $Fe_3O_4$ , which would improve  $T_2$  imaging. Compared with gadolinium-species directly grafting or coating with  $Fe_3O_4$ , interstitial-hollow space of yolk-like  $Fe_3O_4@Gd_2O_3$  nanoplatfrom (YFGN) could effectively reduce the disturbance of  $Fe_3O_4$  for  $T_1$  imaging.

In addition, a yolk-like nanoparticle with high specific surface area remained an attractive drug delivery system (DDS) because this nanoparticle could easily load lots of anticancer drug into its mesopore and interstitial-hollow space.<sup>24</sup> To efficiently deliver the anticancer drug to acidic tumor sites and reduce systemic toxicity, it was necessary to confer nanomedicine on targeting and pH-responsive drug release ability.<sup>25,26</sup>

Until now, some yolk-like nanoplatforms using  $Fe_3O_4$  have been reported, such as yolk–shell  $Fe_3O_4@Au$ ,<sup>27</sup>  $Fe_3O_4@MgSiO_3$ ,<sup>28</sup> and  $Fe_3O_4@SiO_2$ ,<sup>29</sup> but most of them were only used for  $T_2$  MR imaging, which was not beneficial for precise diagnosis of cancer. To obtain multifunctional imaging mode, some of those nanoplatforms also integrated fluorescence imaging or photoacoustic imaging and so on. However, these multifunctional nanoplatforms needed to utilize other imaging devices, which was time consuming and costly.

Herein, we developed a yolk-like nanoplatform using  $Fe_3O_4$  as core and mesoporous  $Gd_2O_3$  layer as shell with large cavity between them, followed by conjugating polyethylene glycol (PEG) and folic acid (FA) onto  $Gd_2O_3$  shell (FA-PYFGN) as tumor targeted  $T_1$ – $T_2$  dual-mode MR CA and DDS. This nanoplatform showed a high longitudinal ( $r_1$ ) ( $7.91 \text{ mM}^{-1} \text{ s}^{-1}$ ) and transverse relaxation rate ( $r_2$ ) ( $386.5 \text{ mM}^{-1} \text{ s}^{-1}$ ), indicating that this nanoplatform could be a good  $T_1$ – $T_2$  dual-mode CA. In addition, cisplatin (CDDP), a widely used anticancer drug against a variety of cancers such as ovarian, breast, and cervical cancer,<sup>24,30</sup> could be efficiently loaded into FA-PYFGN (FA-PYFGN-CDDP, loading capacity: 112 mg/g). Meanwhile, FA-

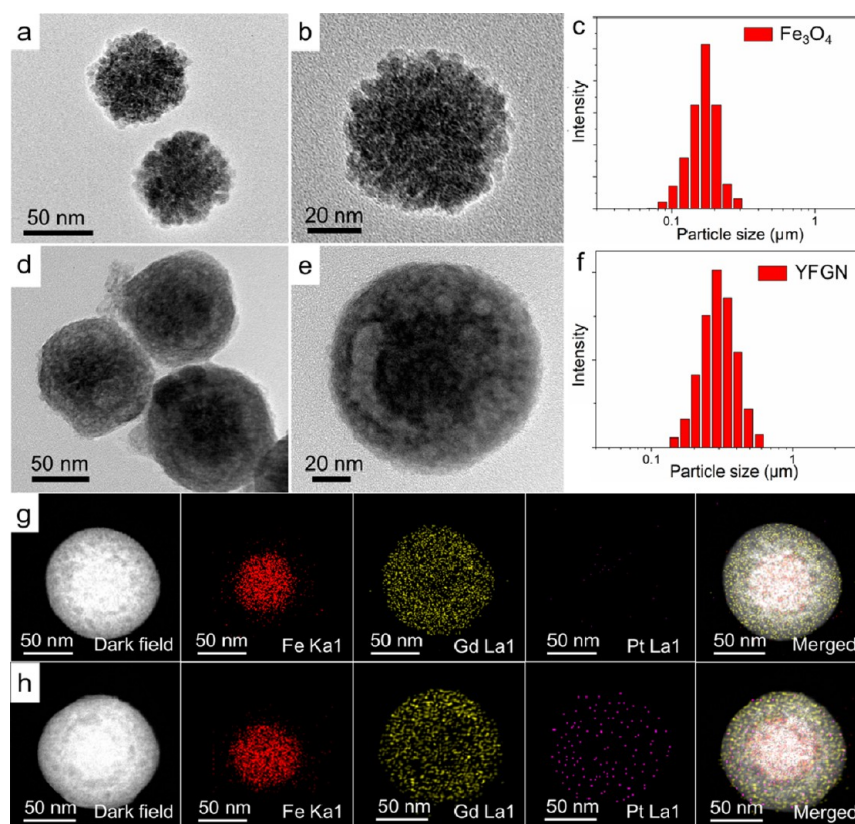


**Figure 2.** TEM images of (a,b)  $\text{Fe}_3\text{O}_4$  and (d,e) YFGN. Hydrodynamic size distribution of (c)  $\text{Fe}_3\text{O}_4$  and (f) YFGN. Scanning TEM images and elemental mapping images of (g) YFGN and (h) YFGN-CDDP.

PYFGN-CDDP displayed a pH-responsive drug release performance. Additionally, *in vitro* and *in vivo*, FA-PYFGN-CDDP could significantly enhance  $T_1$ – $T_2$  dual-mode MR contrast ability and anticancer activity. Importantly, no apparent toxicity for vital organs was observed when systemic delivery of FA-PYFGN-CDDP *in vivo*. Therefore, this nano-platform based on outstanding  $T_1$ – $T_2$  dual-mode MRI and efficient DDS could be a good candidate for the targeted diagnosis and treatment of tumors.

## RESULTS AND DISCUSSION

**Preparation and Characterization of FA-PYFGN-CDDP.** As shown schematically in Figure 1, the preparation process of FA-PYFGN-CDDP was clearly displayed. First, the original  $\text{Fe}_3\text{O}_4$  core was prepared, and then polyethylenimine (PEI) was deposited on its surface. Subsequently, gadolinium precursor could be decomposed and formed gadolinium hydroxide along with PEI chain on the surface of  $\text{Fe}_3\text{O}_4$  at high temperature and pressure conditions. After that, gadolinium hydroxide could further dehydrate and form gadolinium oxide at high temperature and pressure conditions. During the dehydration process, the ordered pore channels in  $\text{Gd}_2\text{O}_3$  shell could be formed.<sup>31,32</sup> In addition, the formation of yolk-like structure was attributed to the existence of dense PEI layer on the surface of  $\text{Fe}_3\text{O}_4$ . After loading CDDP and conjugating PEG and FA to form FA-PYFGN-CDDP, this multifunctional nano-platform with targeting and pH-responsive CDDP release performance would be used as a promising nanotheranostic for  $T_1$ – $T_2$  dual-mode MRI and chemotherapy of cancer *in vivo*.

As seen in transmission electron microscope (TEM) images, the prepared  $\text{Fe}_3\text{O}_4$  core had uniform size (average 57 nm) (Figure 2a,b), and the subsequent prepared YFGN (average 109 nm) showed obvious yolk-like structure with  $\text{Fe}_3\text{O}_4$  core, interstitial-hollow space, and  $\text{Gd}_2\text{O}_3$  shell (Figure 2d,e). Dynamic light scattering (DLS) analysis of  $\text{Fe}_3\text{O}_4$  (average 165 nm, Figure 2c) and YFGN (average 289 nm, Figure 2e) showed narrow peaks, indicating that  $\text{Fe}_3\text{O}_4$  and YFGN possessed homogeneous dispersion. YFGN showed a larger size than that of  $\text{Fe}_3\text{O}_4$  due to the formation of the  $\text{Gd}_2\text{O}_3$  shell. It was noted that hydrodynamic particle sizes of  $\text{Fe}_3\text{O}_4$  and YFGN were larger than that shown in the TEM images, which might be attributed to the aggregation of some nanoparticles in solution. A large number of YFGN nanoparticles could be observed in scanning electron microscope (SEM) images (Figure S1a,b), and the results showed that YFGN possessed uniform size and good dispersity. The scanning TEM and element mapping analysis of YFGN confirmed that Fe and Gd elements were uniformly distributed in the core and shell, respectively (Figure 2g). For YFGN-CDDP, it could be seen that Pt elements were homogeneously distributed in the shell and interstitial-hollow space of YFGN (Figure 2h), indicating that CDDP was successfully loaded into YFGN.

As shown in Figure 3a, YFGN displayed obvious X-ray diffraction (XRD) peaks of the spinel-structure of  $\text{Fe}_3\text{O}_4$  and amorphous  $\text{Gd}_2\text{O}_3$ ,<sup>33,34</sup> confirming the existence of  $\text{Fe}_3\text{O}_4$  and  $\text{Gd}_2\text{O}_3$  in YFGN. In addition, compared to original  $\text{Fe}_3\text{O}_4$ , the diffraction peak of  $\text{Fe}_3\text{O}_4$  in YFGN weakened, which could be assigned to the coverage from  $\text{Gd}_2\text{O}_3$  shell. Thermogravimetric analysis (TGA) of YFGN showed about 45.911% mass loss upon to 800 °C (Figure 3b). Mass loss (15.759%) under 200

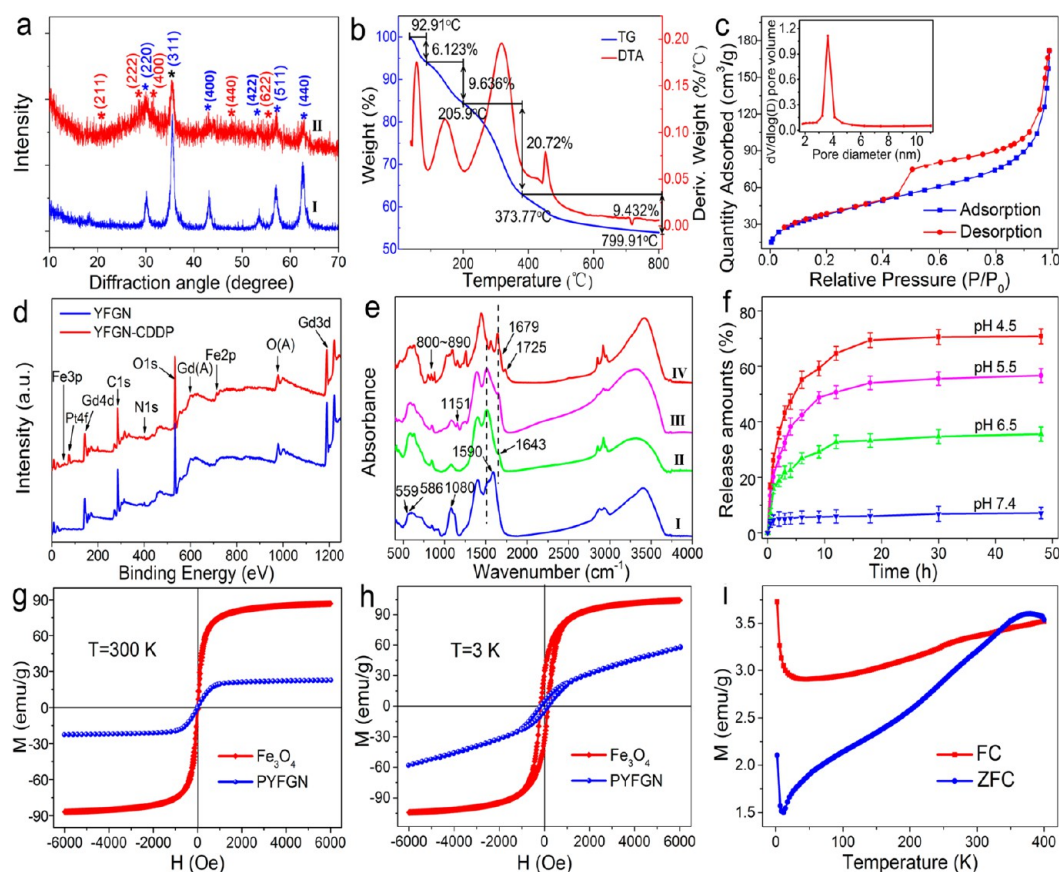


**Figure 3.** (a) XRD patterns of YFGN (I) and  $\text{Fe}_3\text{O}_4$  (II). (b) TGA curves of YFGN. (c)  $\text{N}_2$  adsorption–desorption isotherms of YFGN (inset: pore size distribution). (d) Full XPS spectra of YFGN and YFGN-CDDP. (e) FT-IR spectra of YFGN (I), YFGN-CDDP (II), PYFGN-CDDP (III), and FA-PYFGN-CDDP (IV). (f) Release behavior of CDDP from FA-PYFGN-CDDP under different pH conditions.  $M$ – $H$  curves of  $\text{Fe}_3\text{O}_4$  and PYFGN at 300 K (g) and 3 K (h). (i) ZFC and FC curves of PYFGN.

$^{\circ}\text{C}$  was assigned to the reduction of physically adsorbed water. Mass loss (30.152%) between 200 and 800  $^{\circ}\text{C}$  was due to the burning of organic matters (PEI), indicating that YFGN possessed abundant PEI. Subsequently, the specific surface area and porosity of YFGN were analyzed *via* the nitrogen adsorption–desorption isotherm curves and pore-size distribution curve (Figure 3c). The data showed that YFGN had a high specific surface area (140  $\text{m}^2/\text{g}$ ) and uniform pore size distribution (dominantly 3.9 nm). In the isotherm curve, the typical hysteresis behavior at 0.5–0.9  $P/P_0$  could be attributed to the delay of nitrogen evaporation from the interstitial-hollow space blocked by the surrounding mesopores. These results demonstrated that YFGN was an ideal drug carrier, and the CDDP capacity was 112  $\text{mg}/\text{g}$ .

X-ray photoelectron spectroscopy (XPS) analysis of YFGN (Figure 3d) confirmed the presence of Fe, Gd, O, C, and N elements. The peaks at 1188.9 eV (Gd 3d) and 142.3 eV (Gd 4d) were observed (Figure S2a,b), indicating the existence of  $\text{Gd}_2\text{O}_3$ . While the peak of Fe element at 710.5 eV (Figure S2c) was much lower than that of original  $\text{Fe}_3\text{O}_4$  (Figure S2e,f), which might be attributed to the coverage of  $\text{Gd}_2\text{O}_3$ . Additionally, for YFGN-CDDP, a new peak at 72.7 eV (Pt 4f) appeared (Figure S2g), indicating that CDDP was successfully loaded into YFGN. Moreover, the N 1s peak shifted from 399.8 eV (Figure S2d) to 400.2 eV (Figure S2h), confirming the existence of coordination effect between CDDP and  $\text{NH}_2$  of YFGN. Energy-dispersive X-ray (EDX) analysis also confirmed the presence of Fe, Gd, O, C, N, and Pt

elements in YFGN-CDDP (Figure S3). Afterward, the composition and modification of YFGN were confirmed by the Fourier transform infrared (FT-IR) spectrum (Figure 3e, Figure S4). The peaks at 559, 586, 1590, and 1080  $\text{cm}^{-1}$  were, respectively, assigned to Gd–O stretching vibration, Fe–O stretching vibration, N–H bending vibration, and C–N stretching vibration (Figure 3e(I)), confirming the existence of  $\text{Gd}_2\text{O}_3$ ,  $\text{Fe}_3\text{O}_4$ , and PEI in YFGN. After loading CDDP, N–H bending vibration of YFGN shift from 1590 to 1643  $\text{cm}^{-1}$  (Figure 3e(II)), further confirming the existence of coordination effect between CDDP and  $\text{NH}_2$  of YFGN. When YFGN-CDDP was modified *via* grafting COOH-PEG- $\text{NH}_2$  (Figure 3e(III)), a new peak at 1151  $\text{cm}^{-1}$  appeared, which was assigned to C–O–C stretching vibration of PEG. Compared with PYFGN-CDDP, a new peak at 1725  $\text{cm}^{-1}$  belonging to –COOH stretching vibration and a series of peaks from 800 to 890  $\text{cm}^{-1}$  belonging to the characteristic absorption of phenyl and pterin rings in FA appeared for FA-PYFGN-CDDP (Figure 3e(IV)), indicating FA was successfully conjugated to PYFGN-CDDP.

The release behavior of CDDP from FA-YFGN-CDDP was investigated, and the result indicated that the CDDP release was pH-dependent (Figure 3f). CDDP was hard to be released from FA-PYFGN-CDDP at pH 7.4. However, CDDP release could be promoted under acidic condition, and the release amounts gradually increased with pH decrease. The release mechanism of FA-YFGN-CDDP could be explained as follows: based on preceding analyses, CDDP could be loaded into

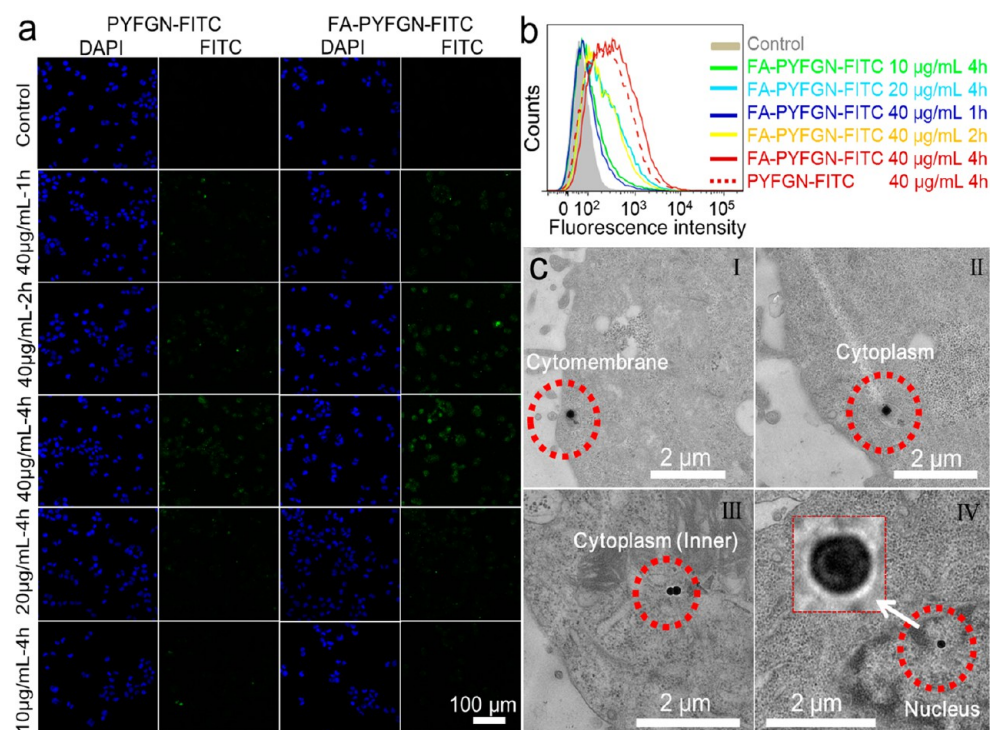


**Figure 4.** (a) CLSM observations of HeLa cells treated with PYFGN-FITC and FA-PYFGN-FITC. For each panel, the images from left to right showed cell nuclei stained by DAPI (blue) and FITC fluorescence in cells (green). All images shared the same scale bar with 100  $\mu\text{m}$ . (b) Flow cytometry analysis of HeLa cells treated with PYFGN-FITC and FA-PYFGN-FITC. (c) TEM observation of HeLa cells treated with FA-PYFGN for 4 h.

YFGN nanoplatfrom *via* coordination effect between  $-\text{NH}_2$  and platinum. However, this interaction could be easily destroyed by the proton attacking because the hydrogen proton easily occupied on the lone pair electrons of the amino group.<sup>35,36</sup> Therefore, the release amount of CDDP from nanoplatfrom was proportional to the concentration of hydrogen proton. Field-dependent magnetization ( $M-H$ ) curves showed that the saturated magnetization value of YFGN (20.9 emu/g) was smaller than that of  $\text{Fe}_3\text{O}_4$  (86.7 emu/g) at 300 K (Figure 3g), this was because of the decrease of  $\text{Fe}_3\text{O}_4$  content per unit mass. In addition, the magnetization of YFGN continuously increased along with the applied magnetic field increase (Figure 3h), which could be due to the enhanced spin canting effect of Gd(III) in  $\text{Gd}_2\text{O}_3$  shell.<sup>37</sup> Standard zero-field cooling (ZFC) and field cooling (FC) measurements of YFGN displayed the similar curves to paramagnetic  $\text{Gd}_2\text{O}_3$  at low temperature and gradually to superparamagnetic  $\text{Fe}_3\text{O}_4$  with increasing temperature (Figure 3i, Figure S5). These magnetic properties of YFGN were similar to nanocomposites containing the high-spin paramagnetic rare-earth materials and superparamagnetic nanoparticles,<sup>38</sup> indicating that superparamagnetic  $\text{Fe}_3\text{O}_4$  and paramagnetic  $\text{Gd}_2\text{O}_3$  were successfully assembled in one nanosystem.

**Observation of Cell Uptake.** Confocal laser scanning microscope (CLSM) was introduced to observe the cell uptake of the nanoplatfrom. HeLa cells treated by PYFGN-FITC and FA-PYFGN-FITC displayed time- and dosage-dependent fluorescence enhancement, respectively (Figure 4a), indicating that cell uptake for this nanoplatfrom was proportional to the incubated time and dosage of particles. Stronger green fluorescence was observed for HeLa cells treated with FA-PYFGN-FITC than that of PYFGN-FITC, indicating that FA-

based targeting strategy was valid for enhancing uptake of nanoplatfrom by HeLa cell. In addition, quantification analysis of HeLa cells by flow cytometric measurements further confirmed that cell uptake for FA-PYFGN-FITC was a dosage- and time-dependent manner (Figure 4b). HeLa cells treated with FA-PYFGN-FITC displayed stronger fluorescence intensity than that of PYFGN-FITC, proving that FA was a good targeting ligand for HeLa cells. Subsequently, the uptake process of FA-PYFGN was directly observed by cell TEM images. As shown in Figure 4c (I–IV), FA-PYFGN nanoparticles were observed on the cytomembrane, cytoplasm, and nucleus. Notably, part of the FA-PYFGN nanoparticles were found in the cellular vesicles (Figure 4c, I and II), indicating the nanoparticles might be taken into HeLa cells *via* endocytosis. Importantly, we could clearly identify the FA-PYFGN nanoparticle with typical yolk-like structure, verifying this nanoplatfrom could keep the good stability in HeLa cell, even in the internalized process. To confirm the good dispersity of particles in cell, the cell CLSM and TEM were investigated. The high-magnification cell CLSM images (Figure S6a–c) showed that lots of green fluorescence points were uniformly distributed into cells, implying that nanoparticles were well-dispersed in cell. Meanwhile, cell TEM image (Figure S6d) intuitively displayed that a large number of particles were taken by HeLa cells and showed good dispersity in cell. Moreover, cell atomic force microscope (AFM) image also showed the existence of single nanoparticle in cell (inset of Figure S6d), which was consistent with TEM results.

**$T_1$ – $T_2$  MR Imaging Performance *in Vitro* and *in Vivo*.** To investigate the MR contrast ability of the nanoplatfrom, PYFGN with different concentration was studied using MR tubes, providing intuitional views by distinguishing brightness ( $T_1$ ) and darkness ( $T_2$ ) of the images. As shown in Figure 5c,

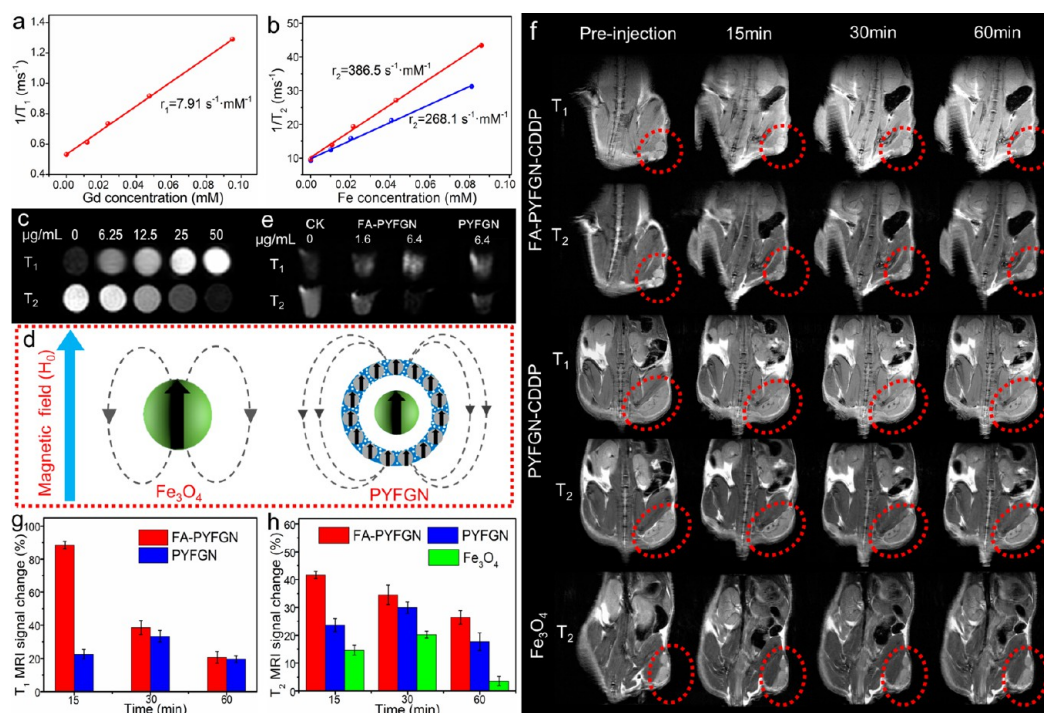


**Figure 5.** (a) The  $r_1$  value of PYFGN and (b)  $r_2$  value of PYFGN and  $\text{Fe}_3\text{O}_4$ . (c)  $T_1$  and  $T_2$  MR images obtained from PYFGN at varied concentrations. (d) Schematic illustration of the enhanced induced magnetic-field of PYFGN. (e)  $T_1$  and  $T_2$  MR images of HeLa cells incubated with FA-PYFGN at varied concentrations for 4 h. (f)  $T_1$ - and  $T_2$ -weighted MR images of mice acquired at pre-injection and post-injection of FA-PYFGN-CDDP and PYFGN-CDDP and corresponding MR  $\Delta\text{SNR}$  (g,h). Tumor marked by red dashed circles.

with increasing concentration of PYFGN,  $T_1$ - and  $T_2$ -weighted MR images gradually brightened and darkened, respectively. Subsequently, corresponding longitudinal ( $r_1$ ) and transverse ( $r_2$ ) relaxivities of PYFGN were, respectively, calculated to be 7.91 and 386.5  $\text{mM}^{-1} \text{s}^{-1}$  (Figure 5a,b), which were higher than those of clinical Gd- or Fe-based CAs.<sup>11,39</sup> Moreover, PYFGN had a higher  $r_2$  value than that of original  $\text{Fe}_3\text{O}_4$  (268.1  $\text{mM}^{-1} \text{s}^{-1}$ ). This might be because the spin order of abundant Gd(III) in the  $\text{Gd}_2\text{O}_3$  shell had the same direction under an external magnetic field,<sup>7,12,40</sup> as shown in schematic illustration (Figure 5d). As a result, a local magnetic field could be formed and overlapped with induced magnetic field of  $\text{Fe}_3\text{O}_4$ , which would increase the magnetic field heterogeneity of  $\text{Fe}_3\text{O}_4$  and further enhance the  $T_2$  contrast effect. MR images of HeLa cells incubated with FA-PYFGN displayed that the  $T_1$ - and  $T_2$ -weighted MR signal intensities gradually improved with increasing FA-PYFGN concentrations (Figure 5e), indicating a dosage-dependent cellular uptake of FA-PYFGN. MR images of HeLa cells incubated with PYFGN at the same concentration (6.4  $\mu\text{g}/\text{mL}$ ) displayed weaker  $T_1$ - and  $T_2$ -weighted MR contrast ability than that of FA-PYFGN. This result also confirmed the enhanced target ability of FA-PYFGN for HeLa cells in comparison to bare PYFGN particles.

To demonstrate the MR contrast effect of nanoplatform *in vivo*, FA-PYFGN and PYFGN (1 mg/kg) were conducted using MRI experiment *via* tail vein injection in tumor-bearing nude mice.  $T_1$ - and  $T_2$ -weighted MR images of interest tumors region were acquired at pre-injection, 15, 30, and 60 min post-injection (Figure 5f). Tumor sites of mice treated with FA-PYFGN displayed the brightest  $T_1$ -weighted and darkest  $T_2$ -weighted MR images at 15 min post-injection, and corresponding signal-to-noise ratio changes ( $\Delta\text{SNR}$ ) were calculated to be 88.53% and 41.71% for  $T_1$  and  $T_2$  imaging, respectively (Figure

5g). These results suggested that FA-PYFGN could be effectively accumulated in the tumor area. After 15 min post-injection,  $\Delta\text{SNR}$  of MR images began to gradually decrease, which could be attributed to excretion of FA-PYFGN by metabolism pathways. However, compared to FA-PYFGN, nontargeted PYFGN displayed a low  $T_1$ - and  $T_2$ -weighted  $\Delta\text{SNR}$  in tumor sites. Meanwhile, the largest  $\Delta\text{SNR}$  in the tumor was 38.69% and 32.84% for  $T_1$  and  $T_2$  imaging, respectively, which was lower than that of FA-PYFGN (Figure 5h). In addition,  $T_2$  contrast ability of  $\text{Fe}_3\text{O}_4$  *in vivo* was also explored in comparison with PYFGN.  $\text{Fe}_3\text{O}_4$  containing the same Fe element content as PYFGN was conducted using MRI experiment for tumor-bearing mice. Results indicated tumor tissue of mouse treated with  $\text{Fe}_3\text{O}_4$  had a weaker  $T_2$ -weighted MR contrast enhancement (the largest  $\Delta\text{SNR}$ : 20.64%) than that of PYFGN.

**Antitumor Effect and Safety Investigation of FA-PYFGN-CDDP.** The biocompatibility of PYFGN was investigated using HeLa and NHLF cells. No significant decrease of the viabilities of HeLa and NHLF cells was observed after they were incubated with a wide range of PYFGN concentrations for 48 h (Figure 6a), indicating that PYFGN had good biocompatibility. After that, the viability of HeLa cells incubated with free CDDP, PYFGN-CDDP, and FA-PYFGN-CDDP was assessed. It could be seen that cellular apoptosis induced by free CDDP, PYFGN-CDDP, and FA-PYFGN-CDDP was proportional to the incubated time and CDDP dosage (Figure 6b,c). In addition, the ability to kill HeLa cells was described as follows: FA-PYFGN-CDDP > PYFGN-CDDP > CDDP, indicating the targeted nanoplatform possessed the strongest inhibiting effect for HeLa cells. Meanwhile, compared with free CDDP, FA-PYFGN-CDDP had very low toxicity for NHLF cells (Figure 6d), and this was because the micro-

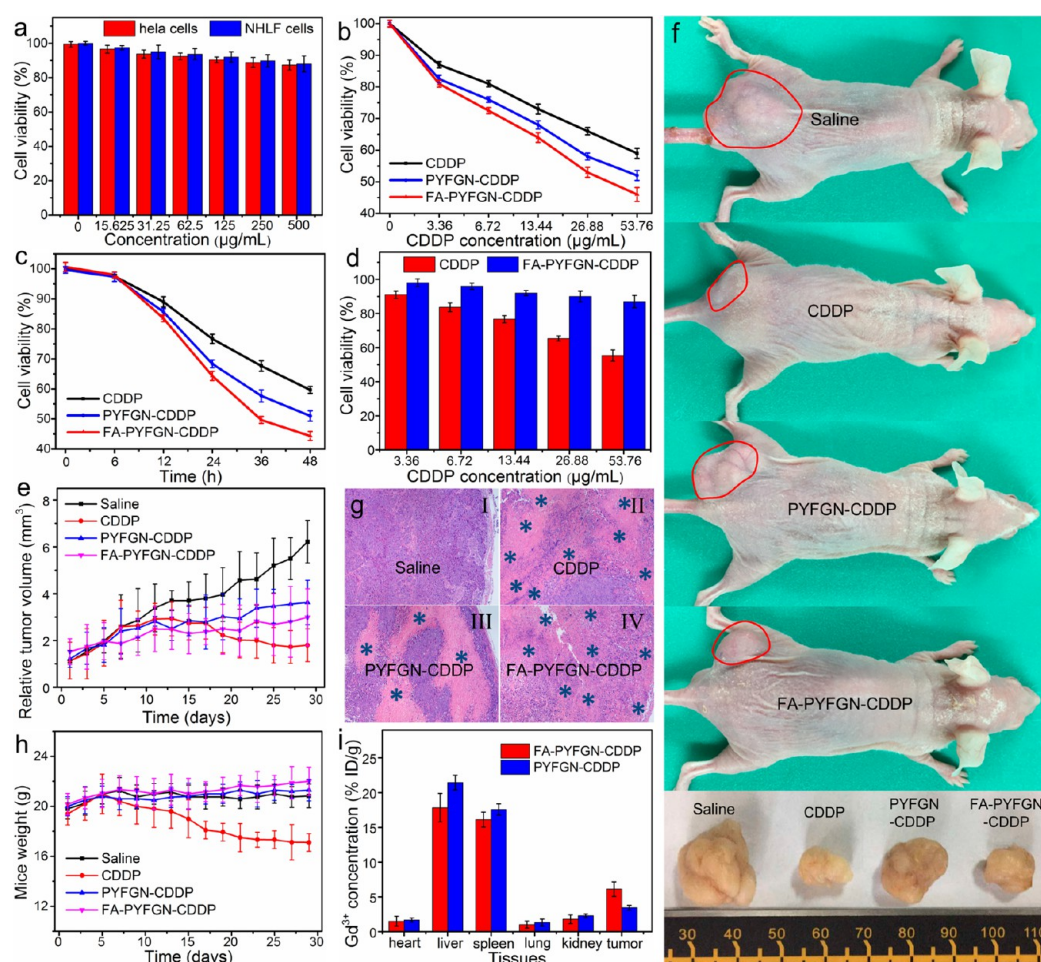


**Figure 6.** (a) Viability of HeLa and NHLF cells treated with different PYFGN concentrations. Viability of HeLa cells treated with free CDDP, PYFGN-CDDP, and FA-PYFGN-CDDP at different CDDP concentrations for 24 h (b) and a different incubation time at the same CDDP concentration (13.44  $\mu\text{g/mL}$ ) (c). (d) Viability of NHLF cells treated with free CDDP and FA-PYFGN-CDDP at different CDDP concentrations for 24 h. (e) Relative tumor volume, (f) representative photographs of mice and excised tumors, (g) H&E staining of tumor tissue, and (h) the body weight changes after tumor-bearing nude mice treated with different samples *via* tail vein injection. (i) The biodistribution of nanoparticles ( $\text{Gd}^{3+}$  concentration) in vital organs of mice harvested at 2 h after intravenous injection of PYFGN-CDDP or FA-PYFGN-CDDP into mice.

environment of NHLF was weakly alkaline and could not trigger the CDDP release. To investigate antitumor efficacy of the nanoplatform *in vivo*, 20 tumor-bearing mice were randomly divided into four groups ( $n = 5$ ) and treated by saline, free CDDP, PYFGN-CDDP, and FA-PYFGN-CDDP *via* tail vein injection, respectively. Compared to saline, all of the other samples showed tumor growth suppression (Figure 6e). FA-PYFGN-CDDP exhibited the best inhibition effect with smallest relative tumor volume before 15 days post-injection, which could be attributed to the targeting accumulation and the sustained CDDP release of the nanoplatform in tumor site. However, the relative tumor volume of mice injected by free CDDP demonstrated a significant decrease after 15 days, which might be because CDDP could cause abnormal functioning of vital organs,<sup>41,42</sup> affecting tumor progression. The final tumor size was also directly observed by photographs of mice and excised tumors (Figure 6f). In addition, the apoptosis of tumor tissue was further evaluated by hematoxylin and eosin (H&E) staining. Compared with saline and PYFGN-CDDP, numerous necrotic areas were shown within tumor tissues of mice treated with FA-PYFGN-CDDP (Figure 6g), indicating that FA-PYFGN-CDDP was an effective antitumor agent. Numerous

necrotic areas were also observed in tumor tissue of mice treated by free CDDP, which might also be because free CDDP has serious side effects to vital organs, causing the apoptosis of tumor tissue.<sup>41,42</sup>

For a better clinical use, it was essential to investigate the leakage of Gd ions from FA-PYFGN-CDDP under different pH conditions because free Gd ions can cause damage to kidneys.<sup>43</sup> Results showed that the leaking amount of Gd ions from FA-PYFGN-CDDP was very low and could be negligible even at pH 5 (Figure S7), indicating FA-PYFGN-CDDP was a stable and safe nanoplatform. The weight change of mice was also evaluated during the process of tumor therapy *in vivo* with different treatment. The body weight of mice treated with saline, PYFGN-CDDP, and FA-PYFGN-CDDP showed no obvious change with increasing time (Figure 6h). However, the body weight of mice treated with free CDDP showed significant decrease with increasing time. These results suggested that free CDDP had serious side effects for mice, and FA-PYFGN-CDDP could effectively reduce the side effects of CDDP for mice. To estimate the biodistribution of nanoplatform *in vivo*, tumor and vital organs were harvested and nitrated with concentrated nitric acid for analyzing Gd ions

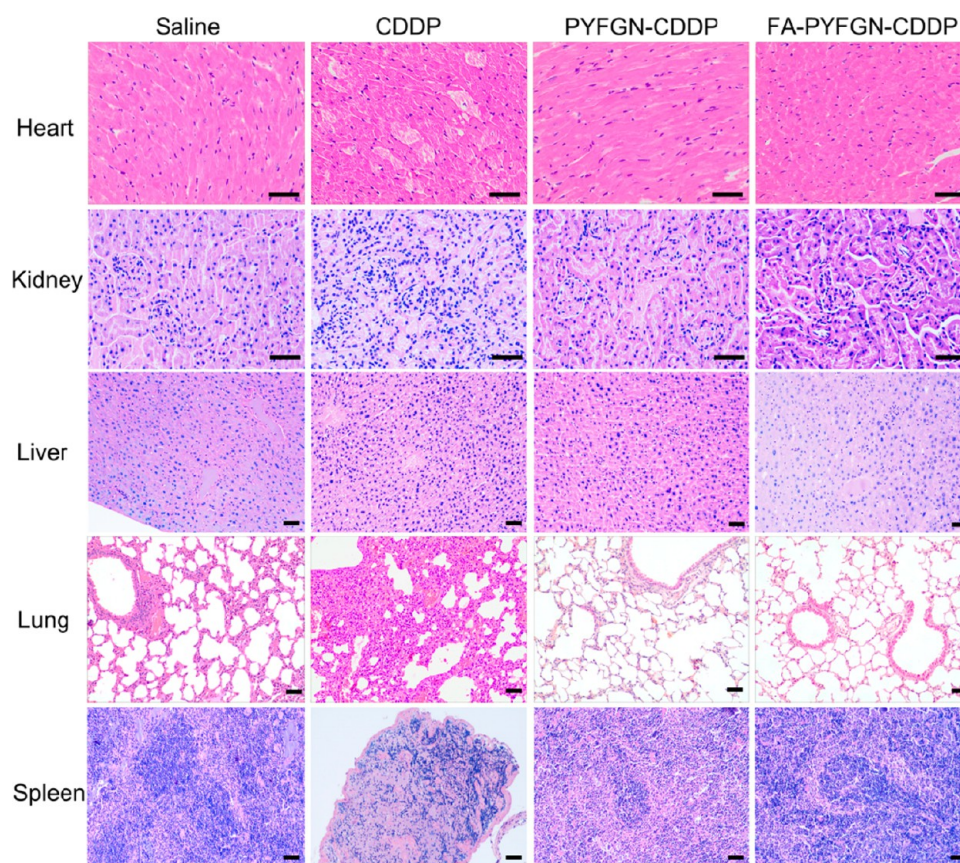


Figure 7. H&E staining of vital organs after tail vein injection of different samples. Scale bar = 100  $\mu\text{m}$ .

amount by inductively coupled plasma optical emission spectrometry (ICP-OES). As shown in Figure 6i, the Gd ion amounts were very low in the heart, lung, and kidney. In sharp contrast, liver and spleen with the reticuloendothelial systems (RES) showed relatively high Gd ion amounts. In addition, for mice treated with FA-PYFGN-CDDP, tumor sites displayed higher Gd ion amounts, but organs with RES showed lower Gd ion amounts than those of PYFGN-CDDP, suggesting that the targeted strategy could reduce the uptake of RES for nanoplatform and enhance accumulation at the tumor site. After the seventh day of injections, the particles in all the organs were much less than the first day (Figure S8). The results revealed that the injected FA-PYFGN-CDDP could be excreted from the mice with a prolonged time.

H&E staining of vital organs (*i.e.*, heart, liver, spleen, lung, and kidney) was conducted to further confirm the safety of nanoplatform *in vivo* (Figure 7). No apparent abnormality of vital organs in the histopathological examination was observed after the mice treated with saline, FA-PYFGN-CDDP, or PYFGN-CDDP. However, evaluation of free CDDP injected groups revealed some damages to vital organs, and the detailed description was as follows: (1) lysis of myocardial myoplasm; (2) infiltration of inflammatory cells in kidney; (3) hydropic degeneration and necrosis of hepatocyte; (4) thickening of the alveolar membrane, hyperemia of capillaries, and exudation of erythrocyte and inflammatory cells in lung; and (5) atrophy in whole spleen and hyperplasia of fibrous tissue. These results suggested free CDDP could cause severe side effects for vital organs, and the nanoplatform could effectively reduce the side effect of CDDP for mice.

## CONCLUSIONS

In summary, we developed a multifunctional nanoplatform of FA-grafted PEGylated yolk-like  $\text{Fe}_3\text{O}_4@\text{Gd}_2\text{O}_3$  and utilized this nanoplatform to obtain a MRI diagnosis and for chemotherapy of tumor. This nanoplatform could be efficiently internalized by HeLa cells with time and dosage dependence. In addition, systemic delivery of this nanoplatform significantly improved the quality of  $T_1$ – $T_2$  MR images *in vivo*. FA-grafted strategy and pH-responsive ability were beneficial to deliver this nanoplatform to tumor tissues and then to release the anticancer drug for killing cancer cells, which could effectively reduce side effects of CDDP for mice. Thus, we believe this multifunctional nanoplatform could be a potential nanotheranostic in the future for accurate diagnosis and targeted therapy of cervical cancer.

## MATERIALS AND METHODS

**Materials.** All chemical reagents were analytical grade and used as received without further purification. Iron acetylacetonate ( $\text{Fe}(\text{acac})_3$ ), gadolinium acetylacetonate ( $\text{Gd}(\text{acac})_3$ ), ethylene glycol, diethylene glycol, triethanolamine, folic acid (FA), and dimethyl sulfoxide (DMSO) were purchased from Sinopharm Co. (Shanghai, China). Polyethylenimine (PEI, MW = 10,000), fluorescein isothiocyanate (FITC), *N*-hydroxysuccinimide (NHS), and *N*-ethyl-*N'*-(3-(dimethylamino)propyl) carbodiimide (EDC) were purchased from Aladdin Co. (Shanghai, China). Cisplatin, 4',6'-diamidino-2-phenylindole (DAPI), and trypan blue were purchased from Sigma-Aldrich Co. (USA). HOOC-PEG-NH<sub>2</sub> (MW = 1000) was purchased from Shanghai Ponsure Biotech, Inc. (Shanghai, China). Cell Counting Kit-8 (CCK-8) was obtained from Dojindo (Japan). All other chemicals were obtained from Sinopharm Co. (Shanghai, China).

**Synthesis of Fe<sub>3</sub>O<sub>4</sub>.** Iron acetylacetonate (0.4 g) was added into the mixed solution of ethylene glycol (15 mL) and diethylene glycol (30 mL) under magnetic stirring at 80 °C for 30 min. Subsequently, PEI (1.0 g) was added into the resulting solution at 80 °C and kept for 30 min. Afterward, triethanolamine (3 mL) was added into mixture solution for 30 min. After that, the transparent solution was transferred into the Teflon-lined stainless steel autoclaves and kept at 200 °C for 24 h. The black product (Fe<sub>3</sub>O<sub>4</sub>) was collected and washed with distilled water and alcohol at least three times.

**Synthesis of YFGN.** Fe<sub>3</sub>O<sub>4</sub> particles (50 mg) were dispersed in ethanol (10 mL) containing PEI (1 g) and stirred at room temperature for 12 h. The product (Fe<sub>3</sub>O<sub>4</sub>@PEI) was collected for further use. Gd(acac)<sub>3</sub> (0.5 g) was added into diethylene glycol (50 mL) and stirred at 80 °C for 30 min. Then, Fe<sub>3</sub>O<sub>4</sub>@PEI was dispersed into the solution with stirring for 30 min. Next, triethanolamine (3 mL) was added into the resulting solution at 80 °C for 30 min. After that, the mixture solution was transferred into the Teflon-lined stainless steel autoclaves and kept at 200 °C for 3 days. The obtained product (YFGN) was collected and washed with water and alcohol at least three times.

**Preparation of FA-PYFGN-CDDP.** YFGN (32 mg) was dispersed into CDDP solution (6 mL, 2 mg/mL) and shaken at room temperature for 24 h, so that CDDP could be loaded into YFGN. After centrifuging at 11,000 rpm for 8 min, the residual CDDP in the supernatant was determined using ICP-OES. The drug capacity of YFGN-CDDP could be calculated according to our previously reported method.<sup>32</sup> After that, NH<sub>2</sub>-PEG-COOH (MW = 1000) was grafted onto YFGN-CDDP via the following methods: NH<sub>2</sub>-PEG-COOH (5 mg) was reacted with NHS (5 mg) and EDC (5 mg) in DMSO for 5 h at room temperature. Then, YFGN-CDDP (10 mg) was added into the mixture solution and stirred overnight, and the obtained particles (PYFGN-CDDP) were collected through centrifugation at 11,000 rpm/min.

Afterward, FA was conjugated onto the surface of PYFGN-CDDP (5 mg) via the following methods: (1) FA (0.5 mg) was activated via adding EDC (1 mg) and NHS (1 mg) into the DMSO solution (5 mL) at room temperature for 4 h; (2) PYFGN-CDDP was dispersed into the mixture solution and stirred for 8 h at the same temperature. The obtained product (FA-PYFGN-CDDP) was collected and washed for subsequent experiments.

**Release Behavior Investigation of FA-PYFGN-CDDP.** Four groups of FA-PYFGN-CDDP (10 mg) were dispersed in phosphate buffer solution (PBS, 5 mL) with different pH (4.5, 5.5, 6.5, 7.4), respectively. Then, the resulting solutions were shaken, and the supernatants were tested with different time intervals (5 min, 10 min, 20 min, 30 min, 40 min, 1, 1.5, 2, 3, 5, and 8 h). The release amount of CDDP from the FA-PYFGN-CDDP was calculated according to our previously reported method.<sup>32</sup>

**MR Experiment.** For MRI, the capability of PYFGN to influence the T<sub>1</sub> and T<sub>2</sub> relaxation time was studied using a 9.4 T/400 mm wide bore scanner (Agilent Technologies, Inc., Santa Clara, CA, USA). The longitudinal (T<sub>1</sub>) and transverse (T<sub>2</sub>) relaxation rates were measured using the inversion recovery method and a multiecho spin echo sequence, respectively. The relaxivity (r<sub>1</sub> and r<sub>2</sub>) was determined by a linear fit of the inverse relaxation time as a function of metal ions concentration, which was determined using ICP-OES.

**Cell Culture and Cytotoxicity Assay.** HeLa and NHLF cells were seeded into 96-well plates and cultured in DMEM medium supplemented with 10% FBS and 1% penicillin/streptomycin at 37 °C in a humidified atmosphere containing 5% CO<sub>2</sub> for 24 h. Then HeLa and NHLF cells were treated with different PYFGN concentrations for 48 h. After that, HeLa cells were treated with various concentrations of CDDP, PYFGN-CDDP, and FA-PYFGN-CDDP for 24 h. HeLa cells were also treated by CDDP, PYFGN-CDDP, and FA-PYFGN-CDDP with the same CDDP concentration (13.44 μg/mL) for different incubation times. In addition, NHLF cells were treated with various concentrations of free CDDP and FA-PYFGN-CDDP for 24 h. After that, the culture media was removed, and the cells were washed with PBS. The number of viable cells was determined by the standard MTT assay.

**Confocal Laser Scanning Microscope Observation.** FITC was labeled onto PYFGN and FA-PYFGN to form PYFGN-FITC and FA-PYFGN-FITC by previously described methods.<sup>12</sup> HeLa cells seeded in 60 mm plates (5 × 10<sup>5</sup> cells/dish) were treated with PYFGN-FITC and FA-PYFGN-FITC (20 μg/mL) for 1, 2, and 4 h and then stained with DAPI for an additional 15 min at 37 °C in the dark. Cells were washed twice with PBS (pH 7.4) and fixed with 4% paraformaldehyde for 30 min. Then, cells were visualized using a confocal microscope (Zeiss LSM710 NLO, Germany). Similarly, HeLa cells seeded in 60 mm plates (5 × 10<sup>5</sup> cells/dish) were treated with various concentrations (10, 20, 40 μg/mL) of PYFGN-FITC and FA-PYFGN-FITC for 2 h. The other processes were the same as described above.

**FITC Accumulation Assay.** HeLa cells seeded in 24-well plates (2 × 10<sup>5</sup> cells/well) were treated with PYFGN-FITC and FA-PYFGN-FITC. Afterward, the extracellular fluorescence was quenched with 0.4% trypan blue for 2 min, and the cells were then trypsinized, washed three times with ice-cold pH 7.4 PBS, resuspended in 350 μL PBS, and measured by flow cytometry (CytoFLEX Beckman-Coulter, USA). The fluorescent intensity was calculated by FlowJo software (TreeStar).

**Cell TEM Observation.** HeLa cells grown in the 24-well plates were treated with FA-PYFGN for 4 h. After being harvested, cells were fixed in 0.1 M Na-phosphate buffer (pH 7.4) containing 2% glutaraldehyde for 1 h. After fixation was placed into 1% OsO<sub>4</sub> at room temperature for 2 h, cells were dehydrated with a graded series of ethanol and embedded in epoxy resin. Areas containing cells were block mounted and cut into ultrathin sections. The sections were stained with uranyl acetate and added citrate and examined with a TEM (JEOL-1230, Tokyo, Japan).

**In Vivo Therapy and Histology Examination.** Cervical cancer model was established through direct subcutaneous injection of 5 × 10<sup>7</sup> HeLa cells into the left rear leg of nude mice. After 3–4 weeks, the cervical tumors were allowed to grow to a uniform size of around 100–200 mm<sup>3</sup>. The mice used for the experiment were treated in accordance with the Ethics Committee Guidelines in University of Science and Technology of China. Animal experiments were randomly assigned to four groups, and each group containing 5 nude mice was treated with saline, free CDDP, PYFGN-CDDP, and FA-PYFGN-CDDP for 2 day intervals via tail vein injection, respectively. The injection dosage of all groups except for the control group were 2 mg (particle mass)/kg (body weight). The volume (V) of tumor was calculated as  $V = a \times b^2/2$ , where “a” and “b” were the longest and shortest diameters of the tumor, respectively. The body weight of mice was recorded at 2 day intervals.

For histology analysis, the mice were sacrificed after 28 days. Vital organs and tumor tissues treated with saline, CDDP, PYFGN-CDDP, and FA-PYFGN-CDDP were excised, fixed in 4% formalin overnight, and then embedded in paraffin. Tissue sections were deparaffinized in xylene, dehydrated in graded alcohols (100%, 95%, 85%, 75%), and washed with distilled water. The sliced tissue sections were stained with standard H&E staining and then analyzed with the inverted fluorescence microscope system.

**Biodistribution of Nanoparticles in Vivo.** The tumor-bearing mice were randomly assigned into two groups and treated with PYFGN-CDDP and FA-PYFGN-CDDP at the same dosage of 20 mg (particle mass)/kg (body weight) via tail vein injection. Subsequently, the mice were sacrificed, and corresponding tumor tissue and vital organs (i.e., heart, liver, spleen, lung, and kidney) were harvested for analyzing Gd ions amount by ICP-OES.

**T<sub>1</sub>–T<sub>2</sub> Weighted MRI of Tumor in Vivo.** For mice MR studies, acquisition parameters were chosen: repetition time (TR) = 370 ms, echo time (TE) = 11.6 ms, field of view (FOV) = 40 mm × 40 mm, matrix size = 192 × 192, slice thickness = 1 mm (12 slices, gap = 0), 1 average, and bandwidth (BW) = 50 kHz. We obtained a series of pre-injection baseline T<sub>1</sub>- and T<sub>2</sub>-weighted MR images prior to two types of CA (PYFGN and FA-PYFGN) injections via tail vein. Post-injection scans were obtained at 15, 30, and 60 min with the same dosage of 1 mg/kg. Across scanning sessions, precise measurements and markers were used to ensure consistent placement of the animal's tumor in the

animal holder and the animal's tumor within the magnet. Pulse oximeter triggering was used for the MRI acquisition to reduce artifacts arising from respiratory movement.

**Characterization.** The morphology and microstructure of the samples were observed through an H-800 TEM with EDX spectroscopy (JEM-ARM200F, JEOL Co., Japan). Particle size distribution measurements were conducted on a DLS detector (Nanotracs Wave II, Microtrac Co., USA). The nitrogen adsorption-desorption isotherm of the YFGN was measured using a porosimetry analyzer (Tristar II, 3020M, Micromeritics, USA). TGA of the YFGN was performed using a thermogravimetric analyzer (Q5000IR, TA Co., USA). The structure and interaction of nanoparticles were analyzed using a X-ray diffraction (XRD) (TTR-III, Rigaku Co., Japan) and a FT-IR spectrometer (iS10, Nicolet Co., USA). Magnetic behavior of the samples was measured by a superconducting quantum interference device (SQUID) magnetometer (Bruker Co., Germany).

## ASSOCIATED CONTENT

### Supporting Information

The Supporting Information is available free of charge on the ACS Publications website at DOI: 10.1021/acsnano.7b02675.

Additional figures of materials characterization for YFGN, Fe<sub>3</sub>O<sub>4</sub>, and YFGN-CDDP; cell CLSM, TEM, and AFM observations; Gd ion leakage studies; and biodistribution studies in the mice (PDF)

## AUTHOR INFORMATION

### Corresponding Authors

\*E-mail: dqcai@ipp.ac.cn.

\*E-mail: zdhyy@ahmu.edu.cn.

\*E-mail: zyw@ipp.ac.cn.

### ORCID

Zhengyan Wu: 0000-0002-8142-1848

### Author Contributions

<sup>†</sup>X.S., R.D., and L.Z. contributed equally to this work.

### Notes

The authors declare no competing financial interest.

## ACKNOWLEDGMENTS

The authors acknowledge financial support from the National Natural Science Foundation of China (nos. 21407151, 81371114, 31370983, 81371190, 81401518, and 31430028), the Key Program of Chinese Academy of Sciences (no. KSZD-EW-Z-022-05), the Youth Innovation Promotion Association of Chinese Academy of Sciences (no. 2015385), and the Science and Technology Service Programs of Chinese Academy of Sciences (nos. KFJ-ST-S-ZDTP-002 and KFJ-SW-ST-S-143), Anhui science and technology plan project (nos. 1604a0802082 and 1401045013), Anhui Province Funds for Distinguished Young Scientists (no. 1508085J08), Key projects of the outstanding young talents in Colleges and Universities (no. gxyqZD2016058) and Young Top-Notch Talent Support Scheme from Anhui Medical University.

## REFERENCES

- Xing, H. Y.; Zhang, S. J.; Bu, W. B.; Zheng, X. P.; Wang, L. J.; Xiao, Q. F.; Ni, D. L.; Zhang, J. M.; Zhou, L. P.; Peng, W. J.; et al. Ultrasmall NaGdF<sub>4</sub> Nanodots for Efficient MR Angiography and Atherosclerotic Plaque Imaging. *Adv. Mater.* **2014**, *26*, 3867–3872.
- Na, H. B.; Song, I. C.; Hyeon, T. Inorganic Nanoparticles for MRI Contrast Agents. *Adv. Mater.* **2009**, *21*, 2133–2148.
- Kim, B. H.; Lee, N.; Kim, H.; An, K.; Park, Y. I.; Choi, Y.; Shin, K.; Lee, Y.; Kwon, S. G.; Na, H. B.; et al. Large-Scale Synthesis of Uniform and Extremely Small-Sized Iron Oxide Nanoparticles for

High-Resolution T<sub>1</sub> Magnetic Resonance Imaging Contrast Agents. *J. Am. Chem. Soc.* **2011**, *133*, 12624–12631.

(4) Salerno, M.; Porqueras, D. S. D. Alzheimer's Disease: The Use of Contrast Agents for Magnetic Resonance Imaging to Detect Amyloid Beta Peptide inside the Brain. *Coord. Chem. Rev.* **2016**, *327–328*, 27–34.

(5) Bae, K. H.; Kim, Y. B.; Lee, Y.; Hwang, J. Y.; Park, H. W.; Park, T. G. Bioinspired Synthesis and Characterization of Gadolinium-Labeled Magnetite Nanoparticles for Dual Contrast T<sub>1</sub>- and T<sub>2</sub>-Weighted Magnetic Resonance Imaging. *Bioconjugate Chem.* **2010**, *21*, 505–512.

(6) Li, F. F.; Zhi, D. B.; Luo, Y. F.; Zhang, J. Q.; Nan, X.; Zhang, Y. J.; Zhou, W.; Qiu, B. S.; Wen, L. P.; Liang, G. L. Core/Shell Fe<sub>3</sub>O<sub>4</sub>/Gd<sub>2</sub>O<sub>3</sub> Nanocubes as T<sub>1</sub>-T<sub>2</sub> Dual Modal MRI Contrast Agents. *Nanoscale* **2016**, *8*, 12826–12833.

(7) Zhou, Z. J.; Huang, D. T.; Bao, J. F.; Chen, Q. L.; Liu, G.; Chen, Z.; Chen, X. Y.; Gao, J. H. A Synergistically Enhanced T<sub>1</sub>-T<sub>2</sub> Dual-Modal Contrast Agent. *Adv. Mater.* **2012**, *24*, 6223–6228.

(8) Yang, H.; Zhuang, Y. M.; Sun, Y.; Dai, A. T.; Shi, X. Y.; Wu, D. M.; Li, F. Y.; Hu, H.; Yang, S. P. Targeted Dual-Contrast T<sub>1</sub>- and T<sub>2</sub>-Weighted Magnetic Resonance Imaging of Tumors Using Multifunctional Gadolinium-Labeled Superparamagnetic Iron Oxide Nanoparticles. *Biomaterials* **2011**, *32*, 4584–4593.

(9) Hu, F. Q.; Zhao, Y. S. Inorganic Nanoparticle-Based T<sub>1</sub> and T<sub>1</sub>/T<sub>2</sub> Magnetic Resonance Contrast Probes. *Nanoscale* **2012**, *4*, 6235–6243.

(10) Estelrich, J.; Sánchez-Martín, M. J.; Busquets, M. A. Nanoparticles in Magnetic Resonance Imaging: From Simple to Dual Contrast Agents. *Int. J. Nanomed.* **2015**, *10*, 1727–1741.

(11) Seo, W. S.; Lee, J. H.; Sun, X.; Suzuki, Y.; Mann, D.; Liu, Z.; Terashima, M.; Yang, P. C.; McConnell, M. V.; Nishimura, D. G.; et al. FeCo/Graphitic-Shell Nanocrystals as Advanced Magnetic-Resonance-Imaging and Near-Infrared Agents. *Nat. Mater.* **2006**, *5*, 971–976.

(12) Zhang, G. L.; Du, R. H.; Zhang, L. L.; Cai, D. Q.; Sun, X.; Zhou, Y.; Zhou, J.; Qian, J. C.; Zhong, K.; Zheng, K.; et al. Gadolinium-Doped Iron Oxide Nanoprobe as Multifunctional Bioimaging Agent and Drug Delivery System. *Adv. Funct. Mater.* **2015**, *25*, 6101–6111.

(13) Johnson, N. J. J.; Oakden, W.; Stanisiz, G. J.; Prosser, R. S.; van Veggel, F. C. J. M. Size-Tunable, Ultrasmall NaGdF<sub>4</sub> Nanoparticles: Insights into Their T<sub>1</sub> MRI Contrast Enhancement. *Chem. Mater.* **2011**, *23*, 3714–3722.

(14) Zhu, L.; Yang, Y.; Farquhar, K.; Wang, J.; Tian, C.; Ranville, J.; Boyes, S. G. Surface Modification of Gd Nanoparticles with pH-Responsive Block Copolymers for Use as Smart MRI Contrast Agents. *ACS Appl. Mater. Interfaces* **2016**, *8*, 5040–5050.

(15) Blanco-Andujar, C.; Walter, A.; Cotin, G.; Bordeianu, C.; Mertz, D.; Felder-Flesch, D.; Begin-Colin, S. Design of Iron Oxide-Based Nanoparticles for MRI and Magnetic Hyperthermia. *Nanomedicine* **2016**, *11*, 1889–1910.

(16) Choi, J.; Lee, J.; Shin, T.; Song, H.; Kim, E.; Cheon, J. Self-Confirming “AND” Logic Nanoparticles for Fault-Free MRI. *J. Am. Chem. Soc.* **2010**, *132*, 11015–11017.

(17) Yang, M. C.; Gao, L. P.; Liu, K.; Luo, C. H.; Wang, Y. T.; Yu, L.; Peng, H.; Zhang, W. Characterization of Fe<sub>3</sub>O<sub>4</sub>/SiO<sub>2</sub>/Gd<sub>2</sub>O<sub>3</sub>(CO<sub>3</sub>)<sub>2</sub> Core/Shell/Shell Nanoparticles as T<sub>1</sub> and T<sub>2</sub> Dual Mode MRI Contrast Agent. *Talanta* **2015**, *131*, 661–665.

(18) Kim, M.; Son, H.; Kim, G.; Park, K.; Huh, Y.; Haam, S. Redoxable Heteronanostructures Functioning Magnetic Relaxation Switch for Activatable T<sub>1</sub> and T<sub>2</sub> Dual-Mode Magnetic Resonance Imaging. *Biomaterials* **2016**, *101*, 121–130.

(19) Santra, S.; Jativa, S. D.; Kaittanis, C.; Normand, G.; Grimm, J.; Perez, J. M. Gadolinium-Encapsulating Iron Oxide Nanoprobe as Activatable NMR/MRI Contrast Agent. *ACS Nano* **2012**, *6*, 7281–7294.

(20) Zhao, W.; Huang, H.; Sun, Y.; Zhang, X.; Li, Y.; Wang, J. T<sub>1</sub>-Weighted and T<sub>2</sub>-Weighted MRI Probe Based on Gd-DTPA Surface Conjugated SPIO Nanomicelles. *RSC Adv.* **2015**, *5*, 97675–97680.

(21) Peng, H. X.; Cui, B.; Li, L. L.; Wang, Y. S. A Simple Approach for the Synthesis of Bifunctional Fe<sub>3</sub>O<sub>4</sub>@Gd<sub>2</sub>O<sub>3</sub>:Eu<sup>3+</sup> Core-Shell Nanocomposites. *J. Alloys Compd.* **2012**, *531*, 30–33.

- (22) Zhou, Z. J.; Wu, C. Q.; Liu, H. Y.; Zhu, X. L.; Zhao, Z. H.; Wang, L. R.; Xu, Y.; Ai, H.; Gao, J. H. Surface and Interfacial Engineering of Iron Oxide Nanoplates for Highly Efficient Magnetic Resonance Angiography. *ACS Nano* **2015**, *9*, 3012–3022.
- (23) Cai, H. D.; An, X.; Wen, S. H.; Li, J. C.; Zhang, G. X.; Shi, X. Y.; Shen, M. W. Facile Synthesis of Gd(OH)<sub>3</sub>-Doped Fe<sub>3</sub>O<sub>4</sub> Nanoparticles for Dual-Mode T<sub>1</sub>- and T<sub>2</sub>-Weighted Magnetic Resonance Imaging Applications. *Part. Part. Syst. Charact.* **2015**, *32*, 934–943.
- (24) Fan, W. P.; Shen, B.; Bu, W. B.; Chen, F.; Zhao, K. L.; Zhang, S. J.; Zhou, L. P.; Peng, W. J.; Xiao, Q. F.; Xing, H. Y.; et al. Rattle-Structured Multifunctional Nanotheranostics for Synergistic Chemo-/Radiotherapy and Simultaneous Magnetic/Luminescent Dual-Mode Imaging. *J. Am. Chem. Soc.* **2013**, *135*, 6494–6503.
- (25) Lv, R. C.; Yang, P. P.; He, F.; Gai, S. L.; Li, C. X.; Dai, Y. L.; Yang, G. X.; Lin, J. A Yolk-like Multifunctional Platform for Multimodal Imaging and Synergistic Therapy Triggered by a Single Near-Infrared Light. *ACS Nano* **2015**, *9*, 1630–1647.
- (26) Chen, Y.; Chen, H. R.; Zeng, D. P.; Tian, Y. B.; Chen, F.; Feng, J. W.; Shi, J. L. Core/Shell Structured Hollow Mesoporous Nanocapsules: A Potential Platform for Simultaneous Cell Imaging and Anticancer Drug Delivery. *ACS Nano* **2010**, *4*, 6001–6013.
- (27) Lin, L. S.; Yang, X.; Zhou, Z.; Yang, Z.; Jacobson, O.; Liu, Y.; Yang, A.; Niu, G.; Song, J.; Yang, H. H.; et al. Yolk-Shell Nanostructure: An Ideal Architecture to Achieve Harmonious Integration of Magnetic-Plasmonic Hybrid Theranostic Platform. *Adv. Mater.* **2017**, *29*, 1606681.
- (28) Wang, Y.; Zhao, R.; Wang, S.; Liu, Z.; Tang, R. *In Vivo* Dual-Targeted Chemotherapy of Drug Resistant Cancer by Rationally Designed Nanocarrier. *Biomaterials* **2016**, *75*, 71–81.
- (29) Jiao, Y.; Sun, Y.; Tang, X.; Ren, Q.; Yang, W. Tumor-Targeting Multifunctional Rattle-Type Theranostic Nanoparticles for MRI/NIRF Bimodal Imaging and Delivery of Hydrophobic Drugs. *Small* **2015**, *11*, 1962–1974.
- (30) Aryal, S.; Hu, C. M. J.; Zhang, L. F. Polymer-Cisplatin Conjugate Nanoparticles for Acid-Responsive Drug Delivery. *ACS Nano* **2010**, *4*, 251–258.
- (31) Zhou, C.; Wu, H.; Huang, C.; Wang, M.; Jia, N. Facile Synthesis of Single-Phase Mesoporous Gd<sub>2</sub>O<sub>3</sub>:Eu Nanorods and Their Application for Drug Delivery and Multimodal Imaging. *Part. Part. Syst. Charact.* **2014**, *31*, 675–684.
- (32) Sun, X.; Cai, C. J.; Wang, Q.; Cai, D. Q.; Qian, J. C.; Chi, Y.; Zheng, K.; Zhang, X.; Zhang, G. L.; Zhong, K.; et al. A Polyethylenimine Functionalized Porous/Hollow Nanoworm as A Drug Delivery System and A Bioimaging Agent. *Phys. Chem. Chem. Phys.* **2016**, *18*, 7820–7828.
- (33) Gao, J. N.; Ran, X. Z.; Shi, C. M.; Cheng, H. M.; Cheng, T. M.; Su, Y. P. One-Step Solvothermal Synthesis of Highly Water-Soluble, Negatively Charged Superparamagnetic Fe<sub>3</sub>O<sub>4</sub> Colloidal Nanocrystal Clusters. *Nanoscale* **2013**, *5*, 7026–7033.
- (34) Yu, S. M.; Cha, J.; Lee, J. K. Synthesis of Eu<sup>3+</sup>-Doped Gd<sub>2</sub>O<sub>3</sub> in Hollow Nanoparticle Structures by Controlled Chemical Etching with Poly(acrylic acid). *RSC Adv.* **2013**, *3*, 16374–16379.
- (35) Zheng, H.; Xing, L.; Cao, Y.; Che, S. Coordination bonding based pH-responsive drug delivery systems. *Coord. Chem. Rev.* **2013**, *257*, 1933–1944.
- (36) Zhang, Y.; Wang, X. J.; Guo, M.; Yan, H. S.; et al. Cisplatin-loaded Polymer/Magnetite Composite Nanoparticles as Multifunctional Therapeutic Nanomedicine. *Chin. J. Polym. Sci.* **2014**, *32*, 1329–1337.
- (37) Morales, M. P.; Veintemillas-Verdaguer, S.; Montero, M. I.; Serna, C. J.; Roig, A.; Casas, L.; Martinez, B.; Sandiumenge, F. Surface and Internal Spin Canting in  $\gamma$ -Fe<sub>2</sub>O<sub>3</sub> Nanoparticles. *Chem. Mater.* **1999**, *11*, 3058–3064.
- (38) Ma, S.; Li, W. F.; Li, D.; Xiong, D. K.; Sun, N. K.; Geng, D. Y.; Liu, W.; Zhang, Z. D. Large Cryogenic Magnetocaloric Effect in the Blocking State of GdAl<sub>2</sub>/Al<sub>2</sub>O<sub>3</sub> Nanocapsules. *Phys. Rev. B: Condens. Matter Mater. Phys.* **2007**, *76*, 144404.
- (39) Mikhaylov, G.; Mikac, U.; Magaeva, A. A.; Itin, V. I.; Naiden, E. P.; Psakhye, I.; Babes, L.; Reinheckel, T.; Peters, C.; Zeiser, R.; et al. Ferri-Liposomes as An MRI-Visible Drug-Delivery System for Targeting Tumors and Their Microenvironment. *Nat. Nanotechnol.* **2011**, *6*, 594–602.
- (40) Huang, C. C.; Tsai, C. Y.; Sheu, H. S.; Chuang, K. Y.; Su, C. H.; Jeng, U. S.; Cheng, F. Y.; Su, C. H.; Lei, H. Y.; Yeh, C. S. Enhancing Transversal Relaxation for Magnetite Nanoparticles in MR Imaging Using Gd<sup>3+</sup>-Chelated Mesoporous Silica Shells. *ACS Nano* **2011**, *5*, 3905–3916.
- (41) Pabla, N.; Dong, Z. Curtailing Side Effects in Chemotherapy: A Tale of PKC $\delta$  in Cisplatin Treatment. *Oncotarget* **2012**, *3*, 107–111.
- (42) Rabik, C. A.; Dolan, M. E. Molecular Mechanisms of Resistance and Toxicity Associated with Platinating Agents. *Cancer Treat. Rev.* **2007**, *33*, 9–23.
- (43) Penfield, J. G.; Reilly, R. F. What Nephrologists Need to Know about Gadolinium. *Nat. Clin. Pract. Nephrol.* **2007**, *3*, 654–668.